Determination of prestress and elastic properties of virus capsids

Ankush Aggarwal[*]

Zienkiewicz Centre for Computational Engineering, Swansea University,
Swansea, SA1 8EN, United Kingdom

Virus capsids are protein shells that protect the virus genome, and determination of their mechanical properties has been a topic of interest because of their potential use in nanotechnology and therapeutics. It has been demonstrated that stresses exist in virus capsids, even in their equilibrium state, due to their construction. These stresses, termed "prestresses" in this study, closely affect the capsid's mechanical behavior. Three methods—shape-based metric, atomic force microscope indentation, and molecular dynamics—have been proposed to determine the capsid elastic properties without fully accounting for prestresses. In this paper, we theoretically analyze the three methods used for mechanical characterization of virus capsids and numerically investigate how prestresses affect the capsid's mechanical properties. We consolidate all the results and propose that by using these techniques collectively, it is possible to accurately determine both the mechanical properties and prestresses in capsids.

I. INTRODUCTION

The protein coat that protects the genome in viruses, called the capsid, has fascinated biologists, physicists, and mechanicians alike. Its varying mechanical properties during assembly and maturation indicate the importance of having the appropriate mechanical conditions for the virus lifecycle. Thus, a better understanding of capsid mechanics could provide new therapeutic targets and advance their use in nanotechnology [1,2].

Virus capsids are assembled from tens to hundreds of similar proteins. Continuum theory is an attractive choice for modeling them because, unlike molecular models, it can be used to simulate them over longer timescales. Interestingly, isotropic continuum elasticity has been successful in describing the mechanical behavior of virus capsids [3–6], and multiple studies modeled capsid as a shell surface [7–10].

There are several overarching questions about the validity of continuum theory at the scale of virus capsids and appropriateness of isotropic versus anisotropic and homogeneous versus heterogeneous treatment. In our recent study, we tried to answer some of these questions [11]. We showed that for continuum theory to be applicable, the molecular level stresses need to be averaged to zero, which also makes the shell continuum description more appropriate than 3D continuum description [11].

The continuum models come with unknown elastic constants. For example, in shell theory, the capsid has an in-plane stiffness Y and Poisson's ratio ν and a bending stiffness κ. In this study, we look at the practical question of determining these elastic stiffnesses, so that the mechanical behavior of capsids can be accurately described. Many previous studies have proposed several different methods to this end. Here,

we focus on three methods: using the capsid shape [12], indentation using atomic force microscopy (AFM) [5,6,13–15], and molecular dynamics [9]. All of these methods are limited to isotropic and homogeneous models, which will remain the remit of this study as well.

In addition to the elastic constants, continuum models also make an inherent assumption about the "stress-free" reference state, with respect to which stresses are calculated. In virus capsids, because of their construction, their equilibrium state is not a stress-free state due to the preexisting stresses called "prestresses." The effect of prestresses on the capsid shape has been studied [7,10,12,16]. However, their effect on the mechanical behavior is not fully understood.

In this study, we aim to reconcile the above three approaches into a consistent framework that can accurately determine the mechanical properties of virus capsids, as well as identify the prestresses originating from two different sources. We hypothesize that to achieve this, results from the three techniques need to be analyzed simultaneously. Therefore, we theoretically and computationally study the three techniques without focusing on determining the stiffness parameters of a specific capsid.

In the next section, we describe our mechanical model, the cases considered, and the numerical discretization used to solve the equations. Then, we present a section on each of the three methods with a background and our analysis. First, we briefly review the relation between capsid shape and elastic parameters and prestresses. Then, we present the results of numerically simulated AFM indentation for varying elastic parameters and prestresses. Third, we describe the relation between molecular dynamics fluctuations and elastic parameters of a shell in a general case. For a spherical shell without prestresses, we derive this relation analytically and verify numerically. For cases with prestresses, we present the numerical results. Finally, we discuss consolidation of all of the results and insights obtained from this study.

─────────
[*]a.aggarwal@swansea.ac.uk

II. MODEL AND DISCRETIZATION

To calculate the mechanical response of a virus capsid, we first present the details of its mechanical model based on thin shell continuum theory.

A. Definition and kinematics

We model the capsid as a closed elastic surface $\mathcal{S} \in \mathbb{R}^3$ parameterized by curvilinear coordinates (s^1, s^2), which map onto the surface. We consider three configurations for the mapping (Fig. 1): the stress-free configuration $s^\alpha \to \bar{X}(s^\alpha)$, the equilibrium configuration $s^\alpha \to X(s^\alpha)$, and the deformed configuration $s^\alpha \to x(s^\alpha)$. Following the standard definitions in differential geometry, the covariant basis vectors are

$$\bar{A}_\alpha = \frac{\partial \bar{X}}{\partial s^\alpha}, \quad A_\alpha = \frac{\partial X}{\partial s^\alpha}, \text{ and } a_\alpha = \frac{\partial x}{\partial s^\alpha}, \quad (1)$$

in the stress-free, equilibrium, and deformed configurations, respectively. Contravariant basis vectors are defined by relations $a_\alpha \cdot a^\beta = \delta_\alpha^\beta$, and metric tensor has covariant components $a_{\alpha\beta} = a_\alpha \cdot a_\beta$, etc. In the deformed configuration, the surface normal is calculated as

$$n = \frac{a_1 \times a_2}{\|a_1 \times a_2\|}, \quad (2)$$

and the curvature tensor is [17]

$$b = \left(-\frac{\partial n}{\partial s^\alpha} \cdot a_\beta\right) a^\alpha \otimes a^\beta = \left(n \cdot \frac{\partial a_\beta}{\partial s^\alpha}\right) a^\alpha \otimes a^\beta. \quad (3)$$

From the curvature tensor, mean and Gaussian curvatures are obtained using relations $H = \frac{1}{2} \operatorname{tr}(b) = \frac{1}{2} b_\gamma^\gamma$ and $K = \det(b) = |b_\alpha^\beta|$, respectively.

The deformation gradient from stress-free to deformed configuration is $\mathbf{F} = \partial x / \partial \bar{X}$, which is calculated as $\mathbf{F} = a_\alpha \otimes \bar{A}^\alpha$—a rank-2 tensor. The right Cauchy-Green deformation tensor is $\mathbf{C} = \mathbf{F}^\top \mathbf{F}$.

B. Elastic energy

In the deformed configuration, the elastic energy of the shell is split into bending and in-plane stretching components and is written as an integral of the strain energy density:

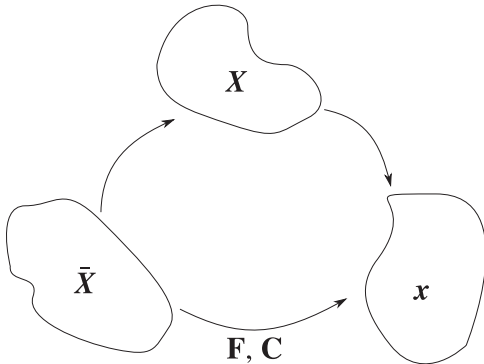$$\Psi(x) = \Psi_b + \Psi_s = \int_{\mathcal{S}} W d\mathcal{S}. \quad (4)$$

FIG. 1. Definition of the deformation gradient and strain tensors between "stress-free" ($\bar{X}$), equilibrium (X), and deformed (x) configurations.

We follow the commonly used assumption that the bending energy vanishes in the flat configuration [7,12] and, therefore, is only dependent on the curvature tensor after deformation:

$$\Psi_b(b) = \int_{\mathcal{S}} \left[\frac{1}{2}\kappa(2H)^2 + \kappa_G K\right] d\mathcal{S}. \quad (5)$$

Furthermore, we only study closed shells, which have the same topology, and by Gauss-Bonnet theorem, the integral of Gaussian curvature remains constant. Thus, for constant κ_G, the second term in the above energy term remains constant under any deformation. Hence, effectively, the bending energy depends only on the mean curvature and bending stiffness κ. It is easy to see that for a closed shell of a given surface area, the bending energy by itself [Eq. (5)] is minimized for a spherical configuration. For the in-plane stretching energy, we use a compressible neo-Hookean model [7,10,18],

$$\Psi_s(\mathbf{C}) = \int_{\mathcal{S}} \left[\frac{\lambda + \mu}{2}(J-1)^2 + \frac{\mu}{2}\left(\frac{\operatorname{tr}(\mathbf{C})}{J} - 2\right)\right] d\mathcal{S}, \quad (6a)$$

where

$$J^2 = \frac{1}{2}\{[\operatorname{tr}(\mathbf{C})]^2 - \operatorname{tr}(\mathbf{C}^2)\}. \quad (6b)$$

The Lamé parameters λ and μ are related to the 2D Young's modulus Y and Poisson's ratio ν via relations

$$\lambda = \frac{Y\nu}{1 - \nu^2} \text{ and} \quad (7a)$$

$$\mu = \frac{Y}{2(1 + \nu)}. \quad (7b)$$

Once linearized for the small displacement case, the neo-Hookean model [Eq. (6)] is equivalent to the St. Venant Kirchhoff's strain energy density function used in the literature [19]. By definition, the equilibrium configuration is the one that minimizes the elastic energy of the shell, i.e.,

$$X = \arg\min_x \Psi(x). \quad (8)$$

C. Cases studied

We study the following three cases for the stress-free configuration $\bar{X}$:

(1) A perfect sphere of radius R is the stress-free configuration [Fig. 2(a)].

(2) A flat hexagonal lattice is the stress-free configuration [Fig. 2(b)], which, following the Caspar-Klug (CK) construction [20], closes into an icosahedron.

(3) The stress-free configuration is obtained after applying a deformation gradient $\mathbf{F}_c$ (called conformational strain) to the flat hexagonal sheet [Fig. 2(c)]. We use a specific form of $\mathbf{F}_c$ observed in several immature capsids [21–25], which is a piecewise constant. That is, $\mathbf{F}_c = \mathbf{1} + \eta u_1 \otimes u_2$ for hexamers (i.e., shear strain η along direction u_1, with u_2 being perpendicular to u_1 and $\mathbf{1} = u_\alpha \otimes u_\alpha$ being the 2D identity tensor) and $\mathbf{F}_c = \mathbf{1}$ for pentamers. As u_1 varies from hexamer to hexamer, it leads to a broken stress-free state [7]. We note that setting $\eta = 0$ gives $\mathbf{F}_c = \mathbf{1}$ everywhere (i.e., zero conformational prestress)
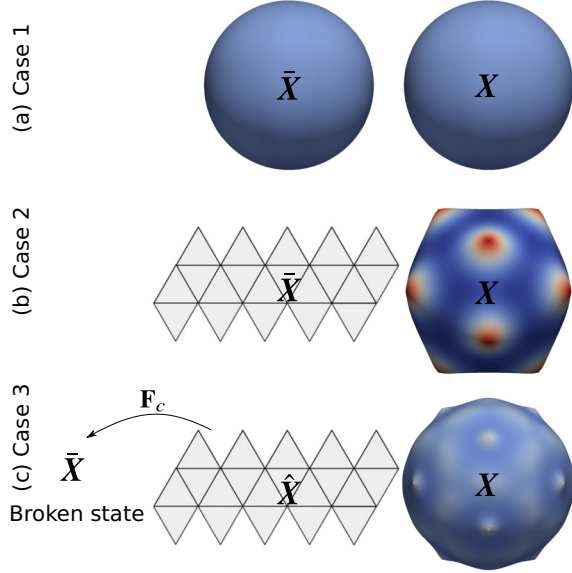
FIG. 2. Depiction of the three cases considered here and their stress-free configurations: (a) no prestress, (b) CK prestress, and (c) conformational prestress. Shells are colored by their radius to emphasize their shape.

and reduces to the second case above. Also, we specifically focus on $\eta = 0.2$, which is the value of shear observed in bacteriophage procapsids [10].

D. Discretization and numerical solution

For numerical calculation of the mechanical response of the shell model, we divide the capsid surface into 26 880 triangles with 13 442 nodes. Therefore, we discretize the position on the capsid surface at time point t as

$$\boldsymbol{x}(s^\alpha; t) = \sum_{I=1}^{N_{\mathrm{nodes}}} N_I(s^\alpha)\boldsymbol{x}_I(t), \qquad (9)$$

where $\boldsymbol{x}_I$ is the position of node I and N_I are the shape functions corresponding to that node (capital indices are used to denote node numbers). We use C^1-continuous subdivision finite element shape functions for the bending energy Ψ_b (5) and C^0-continuous linear Lagrange polynomials for the stretching energy Ψ_s [Eq. (6)]. Interested readers are referred to the literature for more details on these numerical methods [10,26].

III. CAPSID SHAPE

One of the earliest indicators of stiffness parameters was the capsid shape [12,16], and it has been studied in full for all the three cases presented. We present some of the main results here for completeness. We quantify the shape of capsid using asphericity defined as the deviation from a perfect sphere [12],

$$A = \frac{\langle \Delta R^2 \rangle_{\mathcal{S}}}{\langle R \rangle_{\mathcal{S}}^2}, \qquad (10)$$
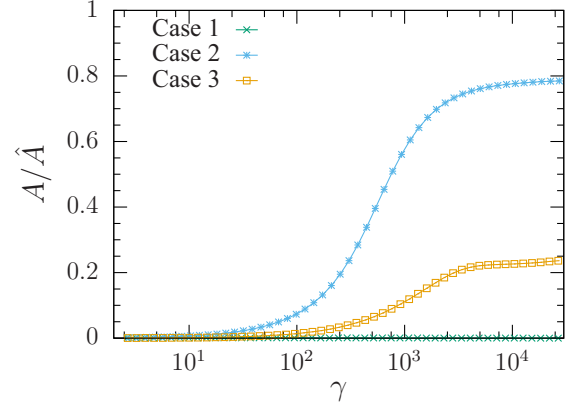

FIG. 3. Normalized asphericity of the capsid as a function of FvK number γ: There is a buckling transition in Case 2, which is significantly reduced in Case 3 with $\eta = 0.2$.

where $\Delta R = R - \langle R \rangle_{\mathcal{S}}$ and angle brackets $\langle \cdot \rangle_{\mathcal{S}}$ denote average over the shell surface. For our finite-element models, these averages are computed over the vertices of the mesh. For reference, we note that $A = 0$ for a perfect sphere and $\hat{A} \approx 0.0026$ for a perfect icosahedron.

The first case we consider is trivial as the capsid shape is a perfect sphere irrespective of its stiffness parameters, i.e., $A = 0$. Since the bending energy is also minimized for a spherical shape, the capsid's equilibrium configuration is also a perfect sphere with energy $\Psi = 8\pi\kappa$, irrespective of its mechanical properties.

For the second case with CK construction, we note that if we disregard the bending energy, the equilibrium shape is a perfect icosahedron with $A \approx 0.0026$. However, since an icosahedron has infinite curvature at its edges (and therefore infinite bending energy), the equilibrium configuration lies somewhere between a sphere and an icosahedron depending on the capsid's stiffness parameters. Specifically, it was shown that the asphericity depends only the dimensionless Föppl von Kármán (FvK) number $\gamma = Y R^2 / \kappa$ (Y and κ are the in-plane and bending stiffnesses and R is the radius) [12]. The 12 pentamers behave as disclination sites because of the construction from a hexagonal lattice, resulting in prestressed pentamers. We call these stresses the CK prestresses after the CK construction of icosahedral capsids [20]. Consequently, the shell goes through a transition from spherical to faceted shape for $\gamma \approx 500$ (Fig. 3). Hence, the capsid shape was proposed to indicate the ratio of its in-plane and bending stiffnesses [12], and a similar result was obtained for nonicosahedral capsids [16].

We recently demonstrated that a similar, and even reverse, shape transition can be driven without changing the mechanical properties, but instead by shearing the individual hexamer units [7], which is the third case. The shear in hexamers, which is observed in several bacteriophage procapsids, adds another prestress (termed as conformational prestress). This additional prestress may release or enhance the CK prestress in pentamers. Hence, it is possible to drive the capsid shape transition via a mechanism independent of its mechanical properties, and this discovery has rendered the shape-based indicator ineffective. Once the shear directions have been

fixed, the equilibrium configuration depends on both FvK number γ and shear η. For $\eta = 0.2$, the shape transition is delayed (at $\gamma \approx 5000$) and severely limited ($A/\hat{A} = 0.2$ only in contrast with 0.8 for Case 2). We have generalized these results to capsids with different protein arrangements and shear directions [10].

IV. AFM INDENTATION

A. Background

A popular experimental technique for estimating the mechanical stiffness of capsids is indentation using atomic force microscopy (AFM) [5,6,13–15], which determines the force f_z versus indentation depth δ response of the whole capsid. Many capsids behave elastically, especially for small indentations, and the effective capsid stiffness is defined as the slope of the force-indentation curve: $k_{cap} = f_z/\delta$. To calculate the continuum elasticity constants, we need to relate them with the effective capsid stiffness.

It is not possible to determine this relation for a general nonlinear elasticity case. For linearized shell theory, $k_{cap} \propto \sqrt{\kappa Y}/R$. In many studies, stiffnesses are related to Young's modulus E through shell thickness h as $Y \sim Eh$ and $\kappa \sim Eh^3$, so that $k_{cap} \propto Eh^2/R$ [5,6]. However, these relations between Y, κ, and E hold true only if the material properties are uniform through the shell thickness, which is not the case for highly heterogeneous molecular systems. As an example, in the case of lipid bilayers, $Y \approx 0$ but κ is finite with a finite shell thickness.

Furthermore, the relation $k_{cap} \propto \sqrt{\kappa Y}/R$ comes from linearized elasticity theory for a perfect sphere, and the effect of prestresses—either CK or conformational—is not included. The effect of CK prestress has only been partially studied; for example, in the case of failure of capsids [8] and release of prestresses [15]. However, its effect on experimental predictions has not been described in full, and the effect of conformational prestress has not been studied. Next, we describe our numerical method to determine these relations.

B. Method

The indentation of the capsid is solved as a quasi-static problem. The substrate is modeled as a rigid flat plate at the bottom and the AFM tip as a rigid hemisphere of radius $R_{tip} \approx R/3$ at the top (Fig. 4). For the spherical stress-free state (Case 1), we indent along any arbitrary axis because of the capsid's spherical symmetry. However, following the CK construction, instead of spherical symmetry, the capsid has an icosahedral symmetry. Therefore, in Cases 2 and 3, the capsid is indented along twofold, threefold, and fivefold symmetry axes. As the AFM tip and substrate (both modeled as rigid bodies) come into contact with the capsid, constraint conditions on the capsid boundary are introduced. The coefficient of friction between the capsid and rigid bodies is set to be high enough ($\mu_f = 1$) to avoid any slipping.

Under AFM indentation, the deformed configuration is determined by numerically minimizing the elastic energy [Eq. (4)] subject to constraints due to contacts between the capsid and AFM tip and substrate. The contact constraint conditions are solved using the augmented Lagrange algorithm
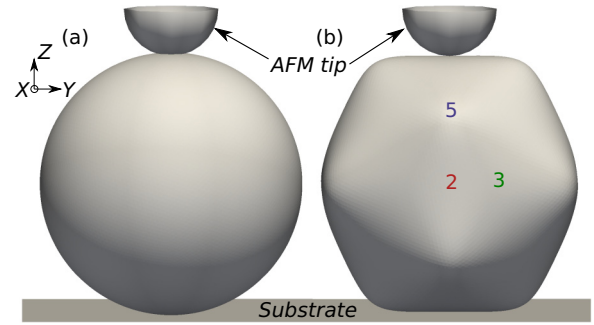

FIG. 4. AFM indentation simulation for (a) spherically symmetric Case 1 and (b) Cases 2 and 3 with icosahedron symmetry using AFM tip radius $R_{tip} \approx R/3$.

([27], Chapter 6). The simulation is repeated for varying values of FvK number γ [between $O(10)$ and $O(10^3)$] and shear η (between -0.3 and 0.3). Based on the linearized theory, the force along indentation direction f_z and indentation depth δ are nondimensionalized using $\sqrt{\kappa Y}$ and R, respectively. Capsid stiffness can be estimated by comparing the experimental and theoretical force-indentation responses.

C. Results

1. Spherical case

Indentation of spherical shells has been investigated in detail [28–30]. For small indentations, the force-indentation relationship follows $f_z/\sqrt{\kappa Y} = \alpha \delta/R$, where α is a proportionality constant that depends on the friction and indentor tip size. Furthermore, the "drop" in the force-indentation relation which denotes a buckling-type event happens whenever the capsid loses contact with the indentor tip or substrate. The number and amount of drops depend on the indentor tip radius [28]. For $R_{tip} \approx R/3$, which is commonly accepted for AFM indentation of capsids, there is no drop (Fig. 5). For small indentation $\alpha \approx 3.3$, independent of the FvK number, which is consistent with previous results [31]. However, we see that
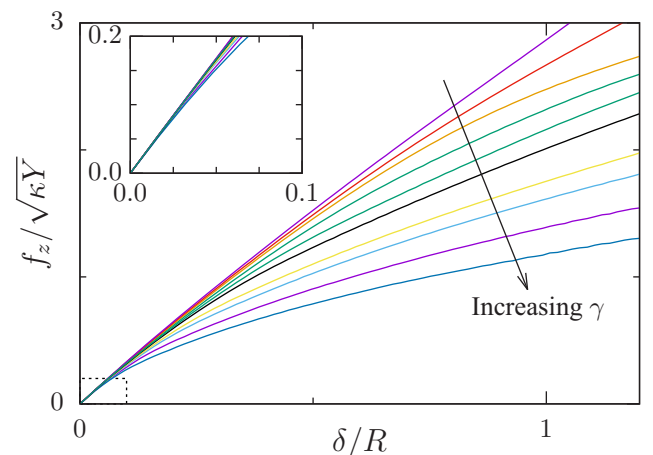

FIG. 5. Nondimensionalized force-indentation curves for a spherical shell (Case 1) with varying FvK number γ. Inset shows zoom-in at small indentation, such that the initial slope is independent of γ.
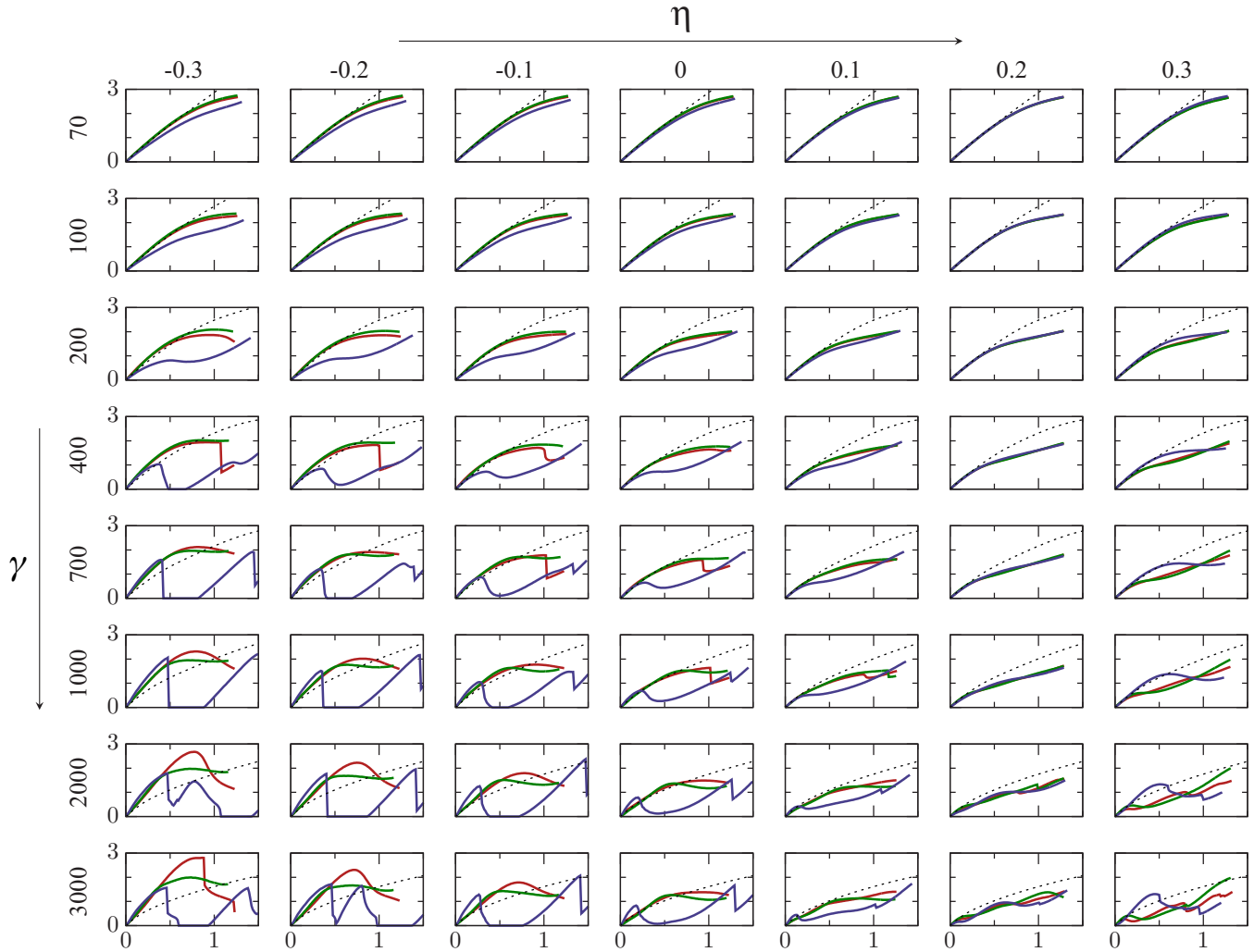
FIG. 6. Nondimensionalized force-indentation curves (vertical axes are $f_z/\sqrt{\kappa Y}$ and horizontal axes are δ/R) for an icosahedral shell with varying FvK number γ and shear η (Cases 2 and 3). Three orientations were simulated: twofold (red), threefold (green), and fivefold (blue). The dashed line shows the response of a sphere without prestresses (Case 1) for comparison.

even a sphere without prestresses shows a softening behavior at large indentations, which becomes more pronounced as we increase γ.

2. Effect of prestress

To study the effect of prestresses, we combine Cases 2 and 3 and simulate indentation for varying values of γ (CK prestress) and shear η (conformational prestress). The results show that, in general, adding prestresses makes the capsid softer at higher indentations compared to the spherical case (Fig. 6). The force-indentation curve for $\eta = 0$ along fivefold axis is different from the twofold and threefold axes, and this difference becomes more prominent at higher γ (Fig. 6). At higher FvK number, the shell goes through a buckling transition when indented along the fivefold axis, but the buckling transition is usually delayed or softened along two- and threefold axes. Rather interestingly, the twofold, threefold, and fivefold curves become almost indistinguishable at $\eta = 0.2$, even at high γ. In general, the variation of shear η, at any given FvK number γ, changes the

relative difference between different orientations minimizing at $\eta = 0.2$.

Furthermore, the initial slope of the nondimensionalized force-indentation curve for twofold and threefold sites remains relatively constant for varying γ and η (Fig. 7). However, the same is not true for the fivefold axis, where the initial slope
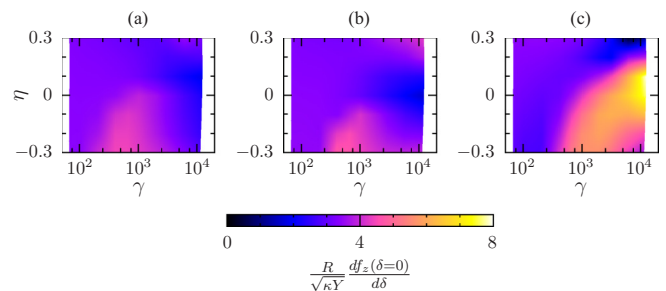

FIG. 7. Nondimensionalized slope for small indentation for an icosahedral shell with varying FvK number γ and shear η (Cases 2 and 3). (a) 2-fold; (b) 3-fold; (c) 5-fold.

becomes more than twice at higher FvK numbers. These results suggest that the relation between effective capsid stiffness and elastic constants depends on prestresses as well as orientation of the indentation, and that a single proportionality relation may lead to inaccurate elastic constants.

V. EQUILIBRIUM FLUCTUATIONS

A. Background

An alternative to using experimental measurements is to calculate the elastic properties of capsid from molecular interactions as proposed by May and Brooks [9]. However, May and Brooks analyzed only the simplest case without any prestresses and ignored nonradial displacements. As a result they could not fit the first two modes, which resulted in inconsistent elastic parameters [11]. Here we extend their approach to a general case and include prestresses.

B. Theory

We assume that we have a molecular dynamics trajectory of the capsid, where the atoms vibrate around the equilibrium state exploring all the microstates. To develop the relationship between molecular dynamics trajectory and elastic properties of the capsid, we define a deformation field $\boldsymbol{u}$ around the equilibrium configuration as

$$\boldsymbol{x}(\boldsymbol{X};t) = \boldsymbol{X} + \boldsymbol{u}(\boldsymbol{X};t). \tag{11}$$

For small displacements, such as those encountered in thermal vibrations, we keep only the lowest (quadratic) order displacement terms in the energy expression. Therefore, the energy change with respect to the minimum energy (i.e., the equilibrium state) is written as

$$\Delta\Psi = \frac{1}{2}\int_{\mathcal{S}} \boldsymbol{u} \cdot \frac{\partial^2 W}{\partial \boldsymbol{u}^2} \cdot \boldsymbol{u} \, d\mathcal{S}. \tag{12}$$

We use $\odot$ to denote the inner product on surface $\mathcal{S}$ as

$$\boldsymbol{v} \odot \boldsymbol{w} = \int_{\mathcal{S}} \boldsymbol{v} \cdot \boldsymbol{w} \, d\mathcal{S}, \tag{13}$$

and $\boldsymbol{v} \cdot \boldsymbol{w} = \sum_i v_i w_i$ represents the Cartesian inner product. We can choose an orthonormal basis for the displacement field $\boldsymbol{U}^i$, i.e., $\boldsymbol{U}^i \odot \boldsymbol{U}^j = \delta_{ij}$, so that the displacement field is written in this basis as $\boldsymbol{u}(\boldsymbol{X};t) = \sum_i \rho_i(t)\boldsymbol{U}^i(\boldsymbol{X})$. An important observation is that if the basis is chosen such that the energy expression can be written as a quadratic sum,

$$\Delta\Psi = \frac{1}{2}\sum_i \rho_i^2 \Lambda_i, \tag{14}$$

for some scalars Λ_i, it becomes possible to invoke the theorem of equipartition. That is, the average value of each term in the above summation equals $k_B T/2$ energy. Thereby, we obtain the expression for time-averaged mode amplitude squared,

$$\langle \rho_i^2 \rangle = \frac{k_B T}{\Lambda_i}, \tag{15}$$

which allows us to relate the molecular dynamics trajectory and elastic model. Comparing Eqs. (12) and (14), it is easy to see that the basis must be the eigenvectors of $\partial^2 W/\partial \boldsymbol{u}^2$ and

Λ_i are the corresponding eigenvalues. Therefore, to relate the thermal vibrations with continuum elastic energy, we need to compute the eigendecomposition.

It is important to note that if there are repeated eigenvalues of multiplicity m corresponding to eigenmodes that are degenerate (for example, related by rotation of the frame of reference), then that eigenmode—combining all its degenerate versions—gets $m k_B T/2$ energy. For example, the rigid translation in three dimensions of any elastic body has three zero eigenvalues, and the thermal energy of the rigid translation is $3k_B T/2$. A similar argument holds for rigid rotations and other eigenmodes with repeated eigenvalues.

For the discretized case with $\boldsymbol{u}(s^\alpha;t) = \sum_I N_I(s^\alpha)\boldsymbol{u}_I(t)$, the energy change becomes

$$\Delta\Psi = \frac{1}{2}\sum_{I,J} \boldsymbol{u}_I^\top \cdot \left(\int_{\mathcal{S}} N_I \frac{\partial^2 W}{\partial \boldsymbol{u}_I \boldsymbol{u}_J} N_J d\mathcal{S}\right) \cdot \boldsymbol{u}_J, \tag{16}$$

and the orthonormality condition becomes

$$\sum_{I,J} \boldsymbol{U}_I^m \cdot \left(\int_{\mathcal{S}} N_I(s^\alpha)N_J(s^\alpha)d\mathcal{S}\right) \cdot \boldsymbol{U}_J^n = \delta_{mn}. \tag{17}$$

We solve this discretized generalized eigenvalue problem numerically using a sparse FEAST solver [32] for γ varying in the range $O(10)$ to $O(10^4)$. For Case 3, the shear is kept constant at a value of 0.2, as per the experimental images of HK97 procapsid—a bacteriophage virus whose hexamers are sheared [7]. The second derivative in Eq. (16) is calculated using central finite difference method.

C. Spherical harmonic decomposition

Different cases may have different eigenfunctions. As we will see that spherical harmonics are the eigenvectors for the case without prestresses (Case 1), that is not true for prestressed shells (Cases 2 and 3). To directly compare different cases, we use spherical harmonics as the common basis to further decompose the equilibrium fluctuations of a general case. Spherical harmonics Y^{lm} of degree $l = 0,\ldots,\infty$ and order $m = -l,\ldots,l$ are defined as the eigenfunctions of Laplace-Beltrami operator ∇^2 on a sphere of radius R

$$R^2\nabla^2 Y^{lm} = -l(l+1)Y^{lm}, \tag{18}$$

and are orthogonal such that $Y^{lm} \odot Y^{l'm'} = R^2\delta_{ll'}\delta_{mm'}$. The radial part [1] of a trajectory can be projected onto the spherical harmonic (SH) basis as

$$\boldsymbol{u}(\boldsymbol{X};t) \cdot \hat{\boldsymbol{r}} = \sum_{l,m} a_{lm}(t)Y^{lm}(\boldsymbol{X}). \tag{19}$$

Therefore, we get

$$\sum_i \rho_i(t)\boldsymbol{U}^i(\boldsymbol{X}) \cdot \hat{\boldsymbol{r}} = \sum_{l,m} a_{lm}(t)Y^{lm}(\boldsymbol{X}), \tag{20}$$

---

[1]Instead of radial part, one could also choose the normal component to be projected onto SH basis. For a spherical surface the radial and normal directions are equivalent ($\boldsymbol{n} = \hat{\boldsymbol{r}}$), and for nonspherical surfaces the difference between two choices was found to be negligible.

and the SH amplitude

$$a_{lm}(t) = \sum_i \rho_i(t) \frac{(\boldsymbol{U}^i(\boldsymbol{X}) \cdot \hat{\boldsymbol{r}}) \odot Y^{lm}(\boldsymbol{X})}{Y^{lm}(\boldsymbol{X}) \odot Y^{lm}(\boldsymbol{X})}. \tag{21}$$

We use the fact that Brownian motion over the surface is completely uncorrelated, i.e., the time-averaged $\langle \rho_i \rho_j \rangle = 0$ for $i \neq j$. Thus, we get a simplified expression for the time-averaged value of the SH amplitude squared (also called SH fluctuation):

$$\langle a_{lm}^2 \rangle = \sum_i \langle \rho_i^2 \rangle \left[\frac{(\boldsymbol{U}^i(\boldsymbol{X}) \cdot \hat{\boldsymbol{r}}) \odot Y^{lm}(\boldsymbol{X})}{Y^{lm}(\boldsymbol{X}) \odot Y^{lm}(\boldsymbol{X})} \right]^2. \tag{22}$$

Denoting the inner product of ith eigenfunction with lm SH,

$$V_i^{lm} = \frac{(\boldsymbol{U}^i \cdot \hat{\boldsymbol{r}}) \odot Y^{lm}}{Y^{lm} \odot Y^{lm}}, \tag{23}$$

using Eq. (15), and summing over order $m = -l, \ldots, l$, we get total fluctuation of SH mode with degree l:

$$\langle a_l^2 \rangle = \sum_{m=-l}^l \sum_i \frac{k_B T}{\Lambda_i} [V_i^{lm}]^2. \tag{24}$$

Hence, given the elastic properties of capsid, its SH fluctuations under thermal excitation can be computed without calculating

a trajectory; one only needs to calculate the eigenfunctions $\boldsymbol{U}^i$ and corresponding eigenvalues Λ_i. Alternatively, the MD trajectory can be directly decomposed to get these fluctuation values, as demonstrated by May and Brooks [9]. A comparison of $\langle a_l^2 \rangle$ from theory and MD provides estimates of capsid elastic parameters (Y, ν, and κ).

D. Spherical case

In this section, we describe the analytical expression for the eigenvectors and eigenvalues for the first case of sphere without any prestresses, as reported by Widom *et al.* [19]. These expressions are then compared to numerical calculations for verification and also used to calculate the spherical harmonic amplitude.

The displacement field on a perfectly spherical surface of radius R can be written using vector spherical harmonics as the basis [19]

$$\boldsymbol{u} = \sum_{l,m} (\xi_L R \, \nabla Y^{lm} + \xi_T R \, \hat{\boldsymbol{r}} \times \nabla Y^{lm} + \xi_r Y^{lm} \hat{\boldsymbol{r}}). \tag{25}$$

When the displacement field Eq. (25) is used in Eq. (12), we get

$$\Delta \Psi = \sum_{l,m} \frac{1}{2} [\xi_T R^2 l(l+1), \xi_L R^2 l(l+1), \xi_r R^2] \cdot \mathcal{H} \cdot \boldsymbol{\xi}, \tag{26}$$

where $\boldsymbol{\xi} = [\xi_T, \xi_L, \xi_r]^\top$ and the expression for the matrix

$$\mathcal{H} = \begin{bmatrix} \mu \frac{(l-1)(l+2)}{R^2} & 0 & 0 \\ 0 & (\lambda+\mu)\frac{l(l+1)}{R^2} + \mu\frac{(l-1)(l+2)}{R^2} & (\lambda+\mu)\frac{2}{R^2} \\ 0 & (\lambda+\mu)\frac{2l(l+1)}{R^2} & (\lambda+\mu)\frac{4}{R^2} + \kappa\frac{l(l-1)(l+1)(l+2)}{R^4} \end{bmatrix} \tag{27}$$

is borrowed from Widom *et al.* [19]. Using the property of vector spherical harmonics, the normalization condition becomes

$$\xi_T^2 R^2 l(l+1) + \xi_L^2 R^2 l(l+1) + \xi_r^2 R^2 = 1. \tag{28}$$

From the definition Eq. (23) we see that $V_i^{lm} = \xi_r \delta_{ll'} \delta_{mm'}$.

1. Radial displacement only

To compare our results with the previous work by May and Brooks [9], we consider the special case when in-plane deformation is restricted to be null $\xi_T = \xi_L = 0$ (i.e., only radial displacement is allowed). Thus, we get

$$\Delta \Psi = \sum_{l,m} \frac{1}{2} \left[(\lambda+\mu)\frac{4}{R^2} + \kappa\frac{l(l-1)(l+1)(l+2)}{R^4} \right] \xi_r^2 R^2. \tag{29}$$

Therefore, we get the eigenvalues for this case:

$$\Lambda_l = (\lambda+\mu)\frac{4}{R^2} + \kappa\frac{l(l-1)(l+1)(l+2)}{R^4}, \tag{30}$$

and, by orthonormality Eq. (28), $\xi_r = V_i^{lm} = 1/R$. Using the relation between Y and μ [Eq. (7b)], the eigenvalues can be

nondimensionalized as

$$\frac{\Lambda_l R^2}{\mu} = 4\left(\frac{\lambda}{\mu} + 1\right) + 2(1+\nu)\frac{l(l-1)(l+1)(l+2)}{\gamma}. \tag{31}$$

Furthermore, for $\nu = 1/3$, we get $\lambda = \mu$, and, thus, $\Lambda_l R^2/\mu = 8 + [8l(l-1)(l+1)(l+2)]/3\gamma$. These can be plotted (Fig. 8) and we see that eigenvalues converge $\Lambda_l R^2/\mu \to 8$ as $\gamma \to \infty \, \forall l$.

Next, using these expressions for eigenvalues and V_i^{lm} in Eq. (24), we get the SH fluctuation:

$$\langle a_l^2 \rangle = \sum_{m=-l}^l \frac{k_B T}{R^2 \Lambda_i} = \sum_{m=-l}^l \frac{k_B T}{(\lambda+\mu)4 + \kappa\frac{l(l-1)(l+1)(l+2)}{R^2}}. \tag{32}$$

We note that the summand is independent of m. Thus, rearranging we get (for $\nu = 1/3$)[2]

$$\frac{\langle a_l^2 \rangle \mu}{k_B T} = (2l+1)\left(8 + \frac{8l(l-1)(l+1)(l+2)}{3\gamma}\right)^{-1}. \tag{33}$$

---

[2] In May and Brooks [9], the contributions from degenerate modes were not summed together, and thus the term $2l+1$ was missing. The analysis presented here and the excellent match with numerical results confirms that this factor is accurate.
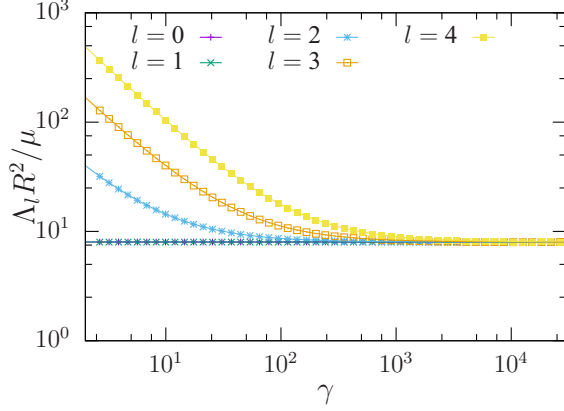
FIG. 8. Nondimensionalized eigenvalues for radial-only motion of a sphere (Case 1) versus FvK number γ (lines are the analytical solution Eq. (31) and points are numerical results showing an excellent fit).

An excellent agreement is obtained when analytical expression is plotted with the numerical solution (Fig. 9). We also note that

$$\lim_{\gamma \to \infty} \frac{\langle a_l^2 \rangle \mu}{k_B T} = \frac{(2l+1)}{8}. \tag{34}$$

2. All displacements allowed

For the general case when in-plane deformations are also allowed, we split the normal modes into purely in-plane modes ($\xi_r = 0$) and those with radial components ($\xi_r \neq 0$). Only the latter contribute to the SH fluctuations $\langle a_l^2 \rangle$. Since the equations involved are cumbersome, the details are presented in the Appendix. Conveniently, vector spherical harmonics are the eigenfunctions. Numerical and analytical solutions of the eigenvalues show an excellent agreement (Fig. 10).

We note that the $l = 0$ degree mode retains its eigenvalue, and thus the fluctuations $\langle a_0^2 \rangle$ remain the same as the previous purely radial case (Figs. 9 and 11). However, the eigenvalue of $l = 1$ degree mode increases by 50% compared to the
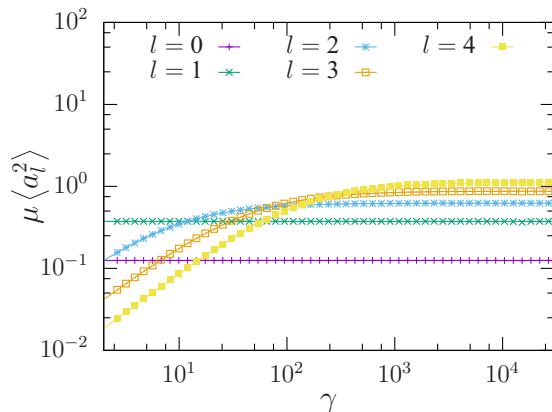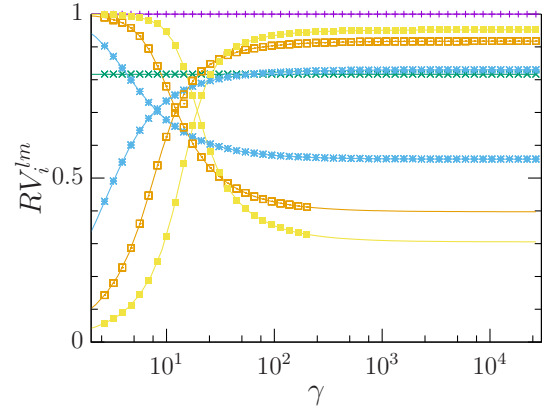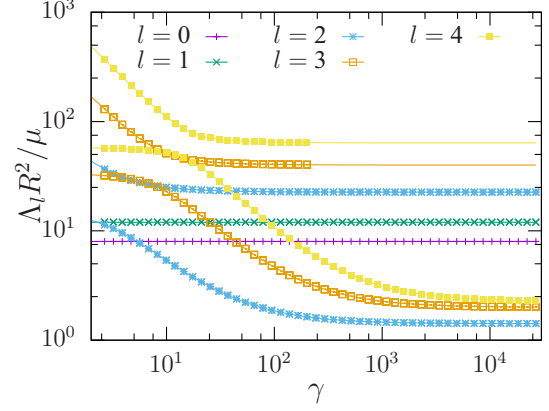

FIG. 10. (Top) Eigenvalues of radial modes and (bottom) their radial component for a sphere (Case 1) versus FvK number γ [lines are the analytical solution Eqs. (A1), (A6), and (A9), and points are numerical results].

purely-radial case, and its equilibrium fluctuations decrease. Also, the eigenvalues do not converge to the same value at large γ (Fig. 10). Both $l = 0$ and 1 modes remain independent of the bending modulus κ. Furthermore, there are two eigenvalues corresponding to each degree l—one lower than the purely radial case and the other higher. Since contribution of each mode to the equilibrium fluctuations is inversely proportional
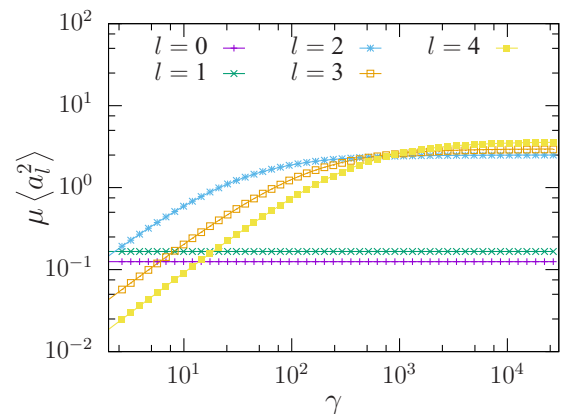

FIG. 9. Spherical harmonic decomposition of equilibrium fluctuations for radial-only motion of a sphere (Case 1) versus FvK number γ (lines are the analytical solution Eq. (33) and points are numerical results).

FIG. 11. Spherical harmonic decomposition of equilibrium fluctuations of a sphere (Case 1) versus FvK number γ [lines are the analytical solution Eq. (A10) and points are numerical results].
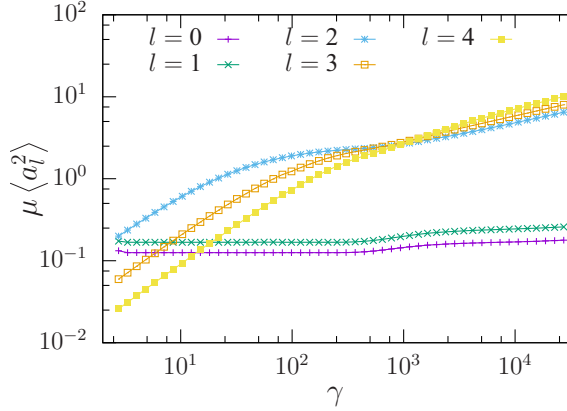
FIG. 12. Spherical harmonic decomposition of equilibrium fluctuations of an icosahedron (Case 2) versus FvK number γ (only numerical results, as analytical solution could not be obtained).

FIG. 13. Spherical harmonic decomposition of equilibrium fluctuations of an icosahedron with conformational prestresses (Case 3) versus FvK number γ (only numerical results, as analytical solution could not be obtained).

to its eigenvalue, $\langle a_l^2 \rangle$ is predominantly decided by the lower frequency modes. As a result, the equilibrium fluctuations for $l \geqslant 2$ increase. Hence, including the in-plane deformations qualitatively changes the normal modes and equilibrium fluctuations.

E. CK prestress

When we follow Caspar-Klug construction and incorporate the associated prestresses, it breaks the spherical symmetry and an analytical solution of eigenfunctions could not be obtained. Thus, we only calculate its eigenvalues and eigenvectors numerically. We find that, because of the lack of spherical symmetry, the eigenvectors are not spherical harmonics (even at low γ), and the eigenvectors cannot be classified into in-plane and radial. In other words, there are no purely in-plane eigenvectors. Therefore, it is difficult to represent the eigenvalues, and we omit its plot for brevity. Nevertheless, we point out one key difference: as γ increases, the lowest eigenvalues do not converge to constant values. Instead, eigenvalues keep decreasing, likely caused by the prestresses at the pentamers. This is reflected in the SH fluctuations (Fig. 12), where $\mu \langle a_l^2 \rangle$ for $l \geqslant 2$ keep increasing even at $\gamma = 10^4$. Furthermore, the fluctuations for $l = 0$ and 1 are not constant over all values of γ. Instead, they show a slight increase at around $\gamma \approx 10^3$, which is close to the transition from spherical to faceted shape.

F. Conformational prestress

When we introduce conformational stresses because of hexamer shearing, an analytical solution of eigenfunctions could not be obtained. Thus, we calculate the eigenvalues, eigenvectors, and SH fluctuations numerically for $\eta = 0.2$ (Fig. 13). Qualitatively, the results are similar to the CK prestress case (Figs. 12 and 13). The main difference is that the transition to higher fluctuation values is shifted towards higher γ, which is consistent with the shape transition also being shifted in this case (Fig. 3).

G. Comparison of three cases

To carefully consider the difference in equilibrium fluctuations between the three cases, we plot them together. First,
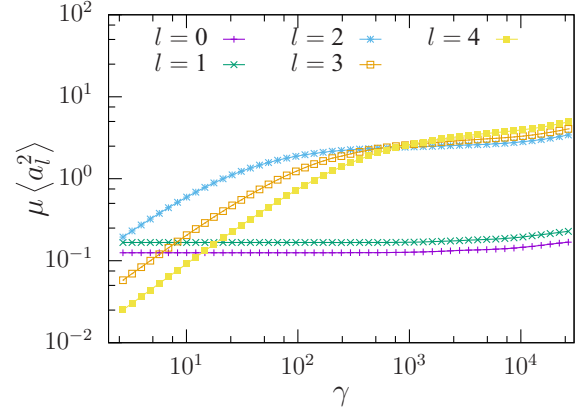
we compare the $\mu \langle a_0^2 \rangle$ (Fig. 14), which remains constant for the spherical case. However, for Cases 2 and 3, it increases slightly at large γ. For Case 2, the increase happens at $\gamma \approx 500$, whereas for Case 3 it happens at $\gamma \approx 5000$. Since the asphericity in Case 3 is less sensitive to γ, we also plot the mode amplitude versus the capsid asphericity (Fig. 14 inset).

Finally, we plot the ratio of fluctuations $\langle a_l^2 \rangle / \langle a_0^2 \rangle$ for $l \geqslant 1$ (Fig. 15). The results indicate that the radial only solution gives significantly different results compared to other cases. Therefore, it is important to account for nonradial deformations in the theory, even if their magnitude is small. Furthermore, the results for Cases 1 and 3 are largely similar. The fluctuations for Case 3 deviate only for large values of γ. In contrast, the fluctuations for Case 2 deviate significantly at large γ and never plateau. Last, we notice that the value of γ at which the relative fluctuations plateau in Cases 1 and 3 increases as we increase the degree l.
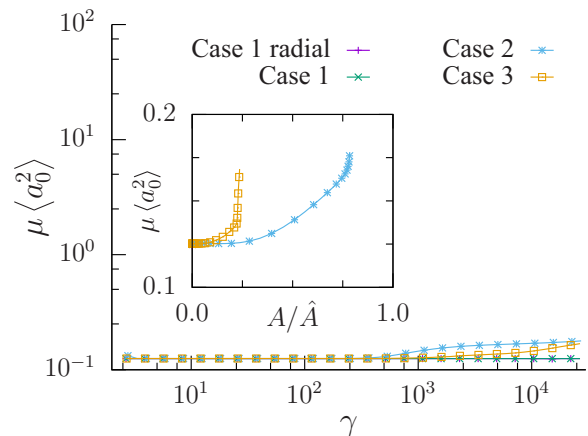

FIG. 14. SH amplitude of degree $l = 0$ is completely insensitive to the FvK number γ for spherical case, whereas for other cases it increases slightly at high FvK number. Inset shows the amplitude as a function of capsid asphericity A normalized by that of a perfect icosahedron $\hat{A}$.
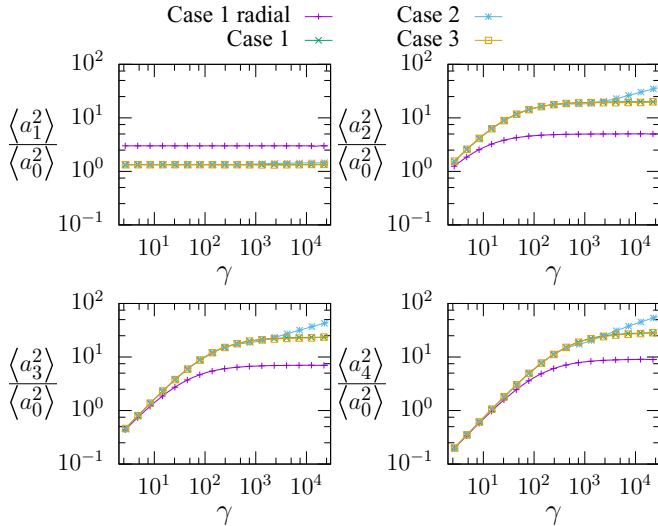
FIG. 15. SH decomposition of all cases for degree $l = 1, 2, 3$, and 4, respectively, normalized by $\langle a_0^2 \rangle$.
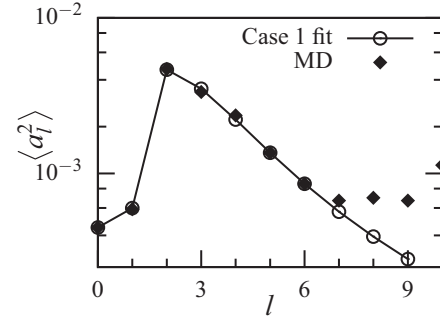

FIG. 16. Case 1 with all displacements [Eq. (A10)] shows an excellent fit to the equilibrium fluctuations of SeMV obtained via MD (taken from Ref. [9]) using a single set of parameters ($Y = 1096.4\ k_B T$, $\kappa = 694\ k_B T/\text{nm}^2$, $\nu = 0.015$, and $\gamma = 130.8$).

VI. DISCUSSION

A. Significance of presented results

In this study, we aimed to carefully analyze the three methods used for determining the mechanical properties of virus capsids in the presence of prestresses. The capsid shape had already been analyzed previously [7,10,12], and the relevant results were summarized. Clearly, in the presence of prestresses, the capsid shape becomes an unreliable indicator of elastic properties.

AFM indentation has been used widely in virus capsid research [5,6,13–15]. However, in determination of the elastic modulus from force-indentation curves, effects of prestresses have been ignored previously [6]. The orientation dependence of the force-indentation curves has been reported previously [5,33]. However, the orientational dependence in those works was ascribed to the geometrical changes with orientation as the prestress was not built into the model. The present results show that prestresses—both CK and conformational—play a role in the force-indentation behavior. Therefore, incorporating prestresses is important when computing elastic modulus based on AFM indentation. Higher stiffness of the force-indentation response along fivefold axis could be seen as an evidence of CK prestresses in virus capsids (Fig. 7). Similarly, the extraneous softening at large indentations may indicate conformational prestresses. However, the effects of prestresses were found to be limited at small FvK values. Last, the results suggest that if the initial slope of the force-indentation curve is used to estimate the elastic moduli, the twofold and threefold axes would provide a better estimate instead of the fivefold axis (because of the prestress concentrations).

For the equilibrium fluctuations, the presented analysis shows that considering the nonradial displacements qualitatively changes the results, and thus it is important to take them into account. Furthermore, the thorough analysis presented here resolves the issue of $l = 0$ and $l = 1$ modes not fitting the MD results [9,34]. As an example, following the analysis presented here, we need only a single set of elastic parameters

for fitting all the SH modes of the Sesbania Mosaic virus's (SeMV) MD trajectory (Fig. 16). The effect of prestresses on equilibrium fluctuations is limited, especially at $\gamma < 5000$, making this approach robust (Fig. 15). These generalizations make this approach an attractive choice for characterizing the capsid mechanics. Furthermore, the numerical scheme presented here can be modified to directly simulate a symmetric unit of the capsid, and therefore intermediary elastic network calculations will not be required as proposed by May and Brooks [9].

B. Combining three methods

We analyzed three methods based on (1) shape of capsid, (2) AFM indentation, and (3) the MD equilibrium fluctuations. It is clear from the results that all three methods have limitations in determining the elastic properties of a capsid. The shape of a capsid was previously used to obtain an estimate of its FvK number; however, that approach becomes ineffective in the presence of conformational stress (Fig. 3). The slope of force-deflection curve from AFM experiments has been extensively used to determine capsid's elastic properties. However, the slope varies depending on the prestresses in the capsid (Fig. 7). The equilibrium fluctuations allow us to determine elastic properties using MD, but they are largely insensitive to small prestresses (Figs. 14 and 15).

To remove the individual limitations of each method, we combine these indicators as follows:

(1) First, we determine the asphericity of the capsid. If the capsid is highly aspherical (i.e., close to perfect icosahedron), then it likely has CK prestress (Case 2) and/or has conformational prestress with negative η (Case 3). For small or intermediate asphericity, it could be any of the cases. If high resolution image of the capsid is available, the value of shear η could be estimated directly.

(2) Second, we determine the FvK number γ and Poisson's ratio ν from the comparison of $\langle a_l^2 \rangle / \langle a_0^2 \rangle$ between MD simulation and theoretical results. Since the theoretical results are nearly same for all cases with $\gamma < 1000$, it is possible to determine γ without distinguishing different cases. However, we note that these curves become relatively flat for $\gamma \gtrsim 5000$ and it is difficult to differentiate FvK values above 5000.

(3) Next, by comparing the asphericity A and FvK number γ determined from previous step, we determine the conformational shear η [10]. We note that this differentiation cannot be made at small FvK values.

(4) Next, we determine μ by comparing the fluctuations $\langle a_l^2 \rangle$ from MD simulation results with the corresponding theoretical results. Using γ, ν, and μ, we determine the bending and in-plane stiffnesses (κ and Y).

(5) Finally, we compare these properties with the initial slope of AFM force-indentation curve. If possible, we use the large indentation response and related softening to differentiate the cases at small γ.

Some of the above steps may have alternatives or could be adjusted based on the information available. Some of the associated limitations are discussed next.

C. Limitations

The presented model does not account for geometric details of the capsid, as those details can also result in orientation dependence of indentation behavior. Incorporating the geometric details into a model with prestress is a challenge that remains to be solved. The analysis presented here is purely theoretical. Even though we consider the practical nature of various methods, there may be additional limitations in combining them. We propose to use behavior at large indentations to identify the conformational prestress. However, some capsids might break before reaching large indentation, limiting that step's practicality. For capsids with $\gamma > 5000$ in Cases 1 and 3, it remains challenging to accurately determine γ as the $\langle a_l^2 \rangle / \langle a_0^2 \rangle$ curves plateau for high FvK numbers.

Some parameters in this study were fixed, and more simulations would be needed to determine their effect on the results. For example, we only studied the conformational prestresses in viruses of HK97 form, which is a $T = 7$ capsid according to CK classification [20]. Although we anticipate that changing the T number would not change the qualitative nature of the

results, this needs to be verified. For thermal fluctuations with conformational prestresses, we fixed $\eta = 0.2$. Similarly, we assumed tip radius $R_{\text{tip}} \approx R/3$ and friction coefficient $\mu_f = 1$ in our AFM simulations. Even though these are acceptable estimates, effect of these parameters on the results remains to be studied to obtain a complete picture. Last, it will be an important step to implement this combined framework for a capsid. However, since that requires both the MD trajectory and AFM experiment, it will be carried out in the future.

D. Conclusion

In this study, we analyzed three different techniques used for determining the elastic properties of virus capsids. Instead of determining the elastic parameters of a specific case, we focused on theoretically analyzing the techniques and the effect of two different kinds of prestress. The results show that using a single technique in isolation can provide contradicting results. Instead, we propose to use them in combination, which can identify not only the elastic properties but also the prestresses. Similar strategies may be valuable to other areas as well, where we combine different methodologies to arrive at consistent and comprehensive results.

APPENDIX: EIGENVALUES AND EQUILIBRIUM FLUCTUATIONS FOR A SPHERE

From Eq. (27), it is easy to see that the purely in-plane modes with $\xi_T = 1/R\sqrt{l(l+1)}$, $\xi_L = \xi_r = 0$ have eigenvalues $\Lambda_l = \mu \frac{(l-1)(l+2)}{R^2}$ (independent of the bending modulus). However, since $\xi_r = 0$, these modes do not contribute to the SH amplitude. Furthermore, for $l = 0$, $\nabla Y_{00} = 0$, resulting in only radial motion $\boldsymbol{u} = Y_{00}\hat{\boldsymbol{r}}$. Thus, we have a purely radial eigenvalue,

$$\Lambda_{l=0} = (\lambda + \mu)\frac{4}{R^2}. \tag{A1}$$

For $l \geqslant 1$ and $\xi_T = 0$, we get

$$\Delta \Psi = \sum_{l,m} \frac{1}{2}[\xi_L R^2 l(l+1), \xi_r R^2] \cdot \mathcal{H} \cdot \boldsymbol{\xi}, \tag{A2}$$

with $\boldsymbol{\xi} = [\xi_L, \xi_r]^\top$ and

$$\mathcal{H} = \begin{bmatrix} (\lambda+\mu)\frac{l(l+1)}{R^2} + \mu\frac{(l-1)(l+2)}{R^2} & (\lambda+\mu)\frac{2}{R^2} \\ (\lambda+\mu)\frac{2l(l+1)}{R^2} & (\lambda+\mu)\frac{4}{R^2} + \kappa\frac{l(l-1)(l+1)(l+2)}{R^4} \end{bmatrix}. \tag{A3}$$

Using $\lambda + \mu = (1+\nu)/(1-\nu)\mu$, the above equation can be rewritten as

$$\mathcal{H} = \frac{\mu}{R^2} \begin{bmatrix} (1+\nu)/(1-\nu)l(l+1) + (l-1)(l+2) & 2(1+\nu)/(1-\nu) \\ 2(1+\nu)/(1-\nu)l(l+1) & 4(1+\nu)/(1-\nu) + l(l-1)(l+1)(l+2)\gamma_\mu^{-1} \end{bmatrix}, \tag{A4}$$

where, for simplifying the expression, we have defined $\gamma_\mu = \mu R^2/\kappa = \gamma/2(1+\nu)$. We note that for each $l \geqslant 1$, we will get two eigenvalues and eigenfunctions from Eq. (A3), each with both radial and in-plane components.

For $l = 1$, the first eigenvalue is $\Lambda^- = 0$—a rigid body translation—and the second eigenvalue is $\Lambda^+ = (\lambda + \mu)\frac{6}{R^2}$ with eigenvector $\xi_r = 2\phi$, $\xi_L = \phi$ and $\xi_T = 0$, where the normalization factor is determined by Eq. (28): $\phi = 1/R\sqrt{l^2 + l + 4} = 1/R\sqrt{6}$. We note that the $l = 1$ mode has increased eigenvalue compared to the purely radial case but is still independent of the bending modulus κ.

To determine the eigenvalues for $l \geqslant 2$, to simplify Eq. (A4), we rewrite as

$$\mathcal{H} = \frac{\mu}{R^2}\begin{bmatrix} a & c \\ d & e + b\gamma_\mu^{-1} \end{bmatrix}, \tag{A5}$$

where $a = (1+\nu)/(1-\nu)l(l+1) + (l-1)(l+2)$, $b = l(l-1)(l+1)(l+2)$, $c = 2(1+\nu)/(1-\nu)$, $d = 2(1+\nu)/(1-\nu)l(l+1)$, and $e = 4(1+\nu)/(1-\nu)$. Thus, defining a new symbol $A = (a - e - \frac{b}{\gamma_\mu})$, the eigenvalues are

$$\frac{\Lambda_l^{\pm}R^2}{\mu} = \frac{1}{2}\left(a + e + \frac{b}{\gamma_\mu} \pm \sqrt{A^2 + 4cd}\right). \tag{A6}$$

We see that for large FvK number, the frequencies do not converge to the same value like they did in the radial-only case. Instead,

$$\lim_{\gamma_\mu \to \infty} \frac{\Lambda_l^{\pm}R^2}{\mu} \to \frac{1}{2}(a + e \pm \sqrt{(a-e)^2 + 4cd}). \tag{A7}$$

Furthermore, the eigenvector is

$$\begin{bmatrix} \xi_L \\ \xi_r \end{bmatrix} = \phi\begin{bmatrix} A \pm \sqrt{A^2 + 4cd} \\ 2d \end{bmatrix}, \tag{A8}$$

where ϕ is determined by the condition Eq. (28). Thus,

$$R^2\xi_r^2 = \frac{4d^2}{8d^2 + 2A^2l(l+1) \pm 2Al(l+1)\sqrt{A^2 + 4cd}}. \tag{A9}$$

The equilibrium fluctuations for each mode will now have contribution from two eigenfunctions corresponding to $\Lambda^{\pm}$. Thus, we get

$$\frac{\langle a_l^2 \rangle \mu}{k_B T} = (2l+1)\left[\frac{8d^2}{\left(a + e + \frac{b}{\gamma_\mu} + \sqrt{A^2 + 4cd}\right)(8d^2 + 2A^2l(l+1) + 2Al(l+1)\sqrt{A^2 + 4cd})}\right.$$
$$\left. + \frac{8d^2}{\left(a + e + \frac{b}{\gamma_\mu} - \sqrt{A^2 + 4cd}\right)(8d^2 + 2A^2l(l+1) - 2Al(l+1)\sqrt{A^2 + 4cd})}\right]. \tag{A10}$$

[1] N. F. Steinmetz, Nanomed.: Nanotechnol. Biol. Med. **6**, 634 (2010).

[2] P. Singh, M. J. Gonzalez, and M. Manchester, Drug Dev. Res. **67**, 23 (2006).

[3] M. M. Gibbons and W. S. Klug, Phys. Rev. E **75**, 031901 (2007).

[4] M. M. Gibbons and W. S. Klug, Biophys. J. **95**, 3640 (2008).

[5] W. H. Roos, M. M. Gibbons, A. Arkhipov, C. Uetrecht, N. R. Watts, P. T. Wingfield, A. C. Steven, A. Heck, K. Schulten, W. S. Klug *et al.*, Biophys. J. **99**, 1175 (2010).

[6] J. P. Michel, I. L. Ivanovska, M. M. Gibbons, W. S. Klug, C. M. Knobler, G. J. L. Wuite, and C. F. Schmidt, Proc. Natl. Acad. Sci. USA **103**, 6184 (2006).

[7] A. Aggarwal, J. Rudnick, R. F. Bruinsma, and W. S. Klug, Phys. Rev. Lett. **109**, 148102 (2012).

[8] W. S. Klug, R. F. Bruinsma, J.-P. Michel, C. M. Knobler, I. L. Ivanovska, C. F. Schmidt, and G. J. L. Wuite, Phys. Rev. Lett. **97**, 228101 (2006).

[9] E. R. May and C. L. Brooks III, Phys. Rev. Lett. **106**, 188101 (2011).

[10] L. Perotti, A. Aggarwal, J. Rudnick, R. F. Bruinsma, and W. S. Klug, J. Mech. Phys. Solids **77**, 86 (2015).

[11] A. Aggarwal, E. R. May, C. L. Brooks, and W. S. Klug, Phys. Rev. E **93**, 012417 (2016).

[12] J. Lidmar, L. Mirny, and D. R. Nelson, Phys. Rev. E **68**, 051910 (2003).

[13] O. Kononova, J. Snijder, M. Brasch, J. Cornelissen, R. Dima, K. Marx, G. L. Wuite, W. Roos, and V. Barsegov, Biophys. J. **105**, 1893 (2013).

[14] W. H. Roos and G. J. L. Wuite, Adv. Mater. **21**, 1187 (2009).

[15] W. S. Klug, W. H. Roos, and G. J. L. Wuite, Phys. Rev. Lett. **109**, 168104 (2012).

[16] T. T. Nguyen, R. F. Bruinsma, and W. M. Gelbart, Phys. Rev. E **72**, 051923 (2005).

[17] F. Feng and W. S. Klug, J. Comput. Phys. **220**, 394 (2006).

[18] E. A. Evans and R. Skalak, CRC Crit. Rev. Bioeng. **3**, 181 (1979).

[19] M. Widom, J. Lidmar, and D. R. Nelson, Phys. Rev. E **76**, 031911 (2007).

[20] D. t. Caspar and A. Klug, in *Cold Spring Harbor Symposia on Quantitative Biology* (Cold Spring Harbor Laboratory Press, Cold Spring Harbor, NY, 1962), Vol. 27, pp. 1–24.

[21] W. Jiang, Z. Li, Z. Zhang, M. L. Baker, P. E. Prevelige, and W. Chiu, Nat. Struct. Biol. **10**, 131 (2003).

[22] T. Dokland, H. Murialdo *et al.*, J. Mol. Biol. **233**, 682 (1993).

[23] P. D. Ross, N. Cheng, J. F. Conway, B. A. Firek, R. W. Hendrix, R. L. Duda, and A. C. Steven, EMBO J. **24**, 1352 (2005).

[24] J. E. Johnson, Curr. Opin. Struct. Biol. **20**, 210 (2010).

[25] A. C. Steven, J. B. Heymann, N. Cheng, B. L. Trus, and J. F. Conway, Curr. Opin. Struct. Biol. **15**, 227 (2005).

[26] F. Cirak and M. Ortiz, Int. J. Numer. Methods Eng. **51**, 813 (2001).

[27] P. Wriggers, *Computational Contact Mechanics* (Springer Science & Business Media, Berlin, 2006).

[28] A. Nasto, A. Ajdari, A. Lazarus, A. Vaziri, and P. M. Reis, Soft Matter **9**, 6796 (2013).

[29] A. Vaziri, Thin-Wall. Struct. **47**, 692 (2009).

[30] A. Vaziri and L. Mahadevan, Proc. Natl. Acad. Sci. USA **105**, 7913 (2008).

[31] G. A. Vliegenthart and G. Gompper, Biophys. J. **91**, 834 (2006).

[32] E. Polizzi, Phys. Rev. B **79**, 115112 (2009).

[33] M. Hernando-Perez, E. Pascual, M. Aznar, A. Ionel, J. R. Caston, A. Luque, J. L. Carrascosa, D. Reguera, and P. J. de Pablo, Nanoscale **6**, 2702 (2014).

[34] E. R. May, A. Aggarwal, W. S. Klug, and C. L. Brooks III, Biophys. J. **100**, L59 (2011).